Detection and Characterisation of a Coronal Mass Ejection using Interplanetary Scintillation measurements from the Murchison Widefield Array

J. Morgan[1], P. I. McCauley[2], A. Waszewski[1], R. Ekers[3,1], R. Chhetri[1,4]

[1]International Centre for Radio Astronomy Research, Curtin University, 1 Turner Avenue, Bentley, WA 6102, Australia
[2]School of Physics, University of Sydney, Sydney, NSW 2006, Australia
[3]CSIRO Space and Astronomy, P.O. Box 76, Epping, NSW 1710, Australia
[4]CSIRO Space and Astronomy, P.O. Box 1130, Bentley, WA 6102, Australia

Key Points:
- We are able to recover a Coronal Mass Ejection detected in coronagraph images in Interplanetary Scintillation (IPS) observations taken 33 hours later.
- The unprecedented number of lines of sight in our IPS observations allow us to image the CME and localise it to degree-level accuracy.
- The CME's location in the IPS observation is consistent with fast-CME propagation, and confirms a 'broadside' (plane of sky) trajectory.

Abstract
We have shown previously that the Murchison Widefield Array (MWA), can detect hundreds of Interplanetary Scintillation (IPS) sources simultaneously across a field of view $\sim 30°$ in extent. To test if we can use this capability to track heliospheric structures, we undertook a search of 88 hours of MWA IPS data, and identified an observation likely to have a significant Coronal Mass Ejection (CME) in the field of view. We demonstrate that in a single 5-minute MWA observation we are able to localise and image a CME $\sim$33 hours after launch at an elongation of $\sim 37°$ from the Sun. We use IPS observables to constrain the kinematics of the CME, and describe how MWA IPS observations can be used in the future to make a unique contribution to heliospheric modelling efforts.

1 Introduction

Interplanetary Scintillation (IPS) is a phenomenon discovered by Clarke (1964) that arises when the turbulent solar wind crosses the line of sight to distant, compact radio sources. As a result, the scintillation signature encodes information on the radio source (Hewish et al., 1964), and the turbulent medium responsible for the scintillation. Early on, IPS was used to track structures out through the heliosphere (Dennison & Wiseman, 1968); many decades before the role of Coronal Mass Ejections (CMEs) in connecting events on the Sun to Space Weather in the near-Earth environment was widely recognised (Gosling, 1993). IPS can also provide velocity measurements of the solar wind; either by the use of multi-station IPS (Dennison & Hewish, 1967) or via fitting the power spectrum measured at a single site. (Young, 1971; Manoharan & Ananthakrishnan, 1990). IPS continues to be used for monitoring of the Solar Wind (see, e.g. Jackson et al., 2020; Tokumaru et al., 2021, and references therein).

Morgan et al. (2018) adapted the IPS technique to exploit the capabilities of widefield interferometers such as the Murchison Widefield Array (MWA; Tingay et al.,

2013), allowing hundreds of IPS sources to be measured simultaneously. Here, we aim to show how this unprecedented number of lines of sight can be used to image structures in the heliosphere. We present the first MWA IPS detection of a CME in the inner heliosphere (c.f. Kaplan et al., 2015, a nightside detection). This observation was selected for analysis from over 1000 observations (Morgan et al., 2019) as a good candidate for containing a CME based on a previous coronagraph detection.

The paper is organised as follows: in Sect. 2 we describe how we chose a target observation and used it to map interplanetary turbulence. In Sect. 3, we describe the CME at launch time, including an analysis of solar coronagraph data to determine a plane-of-sky velocity for the CME after its acceleration. In Sect. 4 we describe the results our of MWA observation, and compare it with near-contemporaneous IPS data from the multi-station ISEE IPS array. In Sect. 5 we analyse these results, and in Sect. 6 we discuss our findings and future plans.

2 Method

2.1 Coordinate systems

For the trajectory of a CME we use a Sun-centred spherical coordinate system where θ refers to the angle with the plane-of-sky (i.e. positive θ is towards Earth, whereas $\theta = 0$ denotes a trajectory normal to the Earth-Sun line) and ϕ is the angle in the plane-of-sky, measured from solar west through north (see Xie et al., 2004, for a more rigorous description). We also use Earth-based observer-centred coordinates, where ϵ is used for solar elongation, and D for the distance from the Earth. ϵ and ϕ together form a heliocentric polar coordinate system for describing the location of any point on the sky relative to the Sun (as observed from Earth). A relationship between ϵ, θ and D can be determined via the sine rule:

$$D\,(\text{AU}) = \frac{\sin\theta'}{\sin(\theta' + \epsilon)} \qquad (1)$$

where $\theta' = \theta - \pi/2$, with the simplifying assumption that the Sun-Earth distance is $1\,\text{AU}$.

2.2 Identification of main target field.

In order to identify MWA IPS observations that were likely to contain a CME, we began with a list of 1062 observations taken between 2015-12-23 and 2016-08-02, described in detail in Morgan et al. (2019). The observations used here cover $154.24\,\text{MHz}$–$169.6\,\text{MHz}$ contiguously, and are $576\,\text{s}$ in duration. Essentially, observations were made of fields offset $30°$ from the Sun, at various position angles. The MWA has a nominal Field of View (FoV) $30°$ across, giving access to solar elongations of $15°$–$45°$. This is a near optimal range for IPS observations at $162\,\text{MHz}$ (an observing frequency which we have chosen to provide a good balance of sensitivity and field of view), and also places the Sun in the null of the instrumental response, mitigating its impact.

For a list of CME events that might be detectable in an MWA IPS observation, we used the catalogue generated by the Computer Aided CME Tracking algorithm (CACTus; Robbrecht & Berghmans, 2004) using images from the Large Angle Spectral Coronagraph (LASCO; Brueckner et al., 1995). This publically available catalogue is described by Robbrecht et al. (2009), and provides a launch time, plane-of-sky velocity, opening angle, and a position angle for each CME. Assuming that all of these CMEs continued to propagate at the velocity determined by CACTus, and utilising the opening angle, we were then able to determine which CMEs would have some overlap with the MWA FoV (note that this analysis predates the publication of CMEChaser (Shaifullah et al., 2020) which takes a broadly similar approach). This method is not intended to be highly accurate, but is a simple and practical way for us to triage our data in an automated fashion. It is nonetheless sufficient for our purposes since with the wide field of view of the MWA, we have a good chance of capturing the CME, even with an error approaching $\pm50\%$.

These very broad criteria resulted in 417 matches between observations and CMEs. Of these, the most promising matches were 21 for which the projected centroid position was within the MWA FoV, and the opening angle covered the entire MWA FoV. This was a small enough number that each crossmatch could be inspected manually. A candidate was chosen on the basis of a predicted location of the CME close to the centre of the FoV, and an unambiguous and strong detection in LASCO difference images. The CACTus CME corresponding to our chosen MWA observation is number 0045 in the CACTus "quick look" catalogue for 2016-05, with a launch time of 2016-05-15T15:24 (see Figure 1).

2.3 The target observation

The corresponding MWA observation began at 2016-05-17T00:25:35 UTC, 33 hours after the CME launch time. Calibration, imaging, and determination of the scintillation index of each IPS sources was then carried out exactly as described in Morgan et al. (2018). We note that due to the unique capabilities of the MWA, the methodology used (in particular, measurement of the thermal noise, and derivation of the scintillation index) differs considerably from that used at other IPS observatories. The method is summarised below, and the reader is referred to Morgan et al. (2018) for further details.

Briefly, a "standard image" was made using the full observation, using standard interferometry software, WS-CLEAN; (Offringa et al., 2014; Offringa & Smirnov, 2017). Images had 2400×1 arcmin pixels in both dimensions, and a uniform visibility weighting scheme was used to maximise image fidelity and resolution. Next, individual snapshot images were made of each 0.5-s observing interval with the same image dimensions, but with a natural weighting scheme to maximise sensitivity. A filter with a bandpass of $0.1\,\text{Hz}$–$0.5\,\text{Hz}$ was then applied to the timeseries corresponding to each pixel. This has the effect of emphasising the IPS signal relative to the noise while eliminating variability due to ionospheric effects. The standard deviation of these filtered timeseries (one per pixel) gives the "variability image", from which can be derived the variance due to IPS alone, with instrumental white noise being measured and subtracted using the majority of pixels which do not contain an IPS source. The noise-subtracted measurement of the brightness of each source in the variability image, along with its brightness in the "standard image", provides the numerator and denominator of the scintillation index.

2.4 The reference observation

Changes in solar wind density along a line of sight to an IPS source causes a change in the scintillation index relative to a baseline level: the so-called 'g-level' (e.g. Gapper et al., 1982). This g-level can then be mapped to a particular density (e.g. Tappin, 1986), though this is not directly relevant to the current work. Since the baseline scintillation level of a particular source cannot be known *a priori*, it is typically determined over a number of days in order to average over stochastic fluctuations.

Most of the IPS sources detected in our target observation are not known IPS sources, and so their typical scintillation level cannot be known *a priori*. For this initial demonstration, we adopt the simple approach of using just a single observation of the same field from 24 hours previously; thus, the g-level for a particular source is simply the ratio of the scintillation index (calculated as described in Sect. 2.3) between the target and reference observations. We do not expect the reference observation to contain a CME according to the cross-match described in Sect. 2.2. This does not preclude structure which escaped classification by CACTus; however it is unlikely that an event as significant as ours would be missed.

Balancing the risk of other heliospheric transients contaminating our reference observation, this approach has several advantages. First, the Sun has only moved $\sim 1°$ relative to our IPS radio sources, a negligible change in elongation. Furthermore, slower variations in the heliosphere, such as the locations of fast and slow streams, will remain roughly constant over 24 hours, and so our calculated g-levels will reflect only the transient changes in the heliosphere which we wish to detect.

3 Ancillary data

In order to characterise the CME as fully as possible, we identified relevant events in the Solar and Geophysical event list published by the Space Weather Prediction Center (SWPC). We also acquired Geostationary Operational Environmental Satellites (GOES) soft X-ray timeseries data and LASCO images. Contemporaneous IPS data from the ISEE IPS array in Japan is described in Sect. 4.1.

The relevant findings are summarised in Figure 1. The SWPC event list recorded a Type III radio burst, a C-class X-ray flare and an Hα solar flare, all of which are likely related to the CME. Importantly, the Hα flare is localised to heliolatitude 10° N, heliolongitude 62° W. This corresponds to a radial trajectory $\phi = 10°$ (north

of West), $\theta = +28°$ (from the plane of sky towards the Earth).

While the CACTus CME parameters were sufficient for the cross-matching process described in Sect. 2.2, we decided to cross-check by performing our own analysis on the original coronagraph images. The CME leading edge was well-defined in 5 C2 images and 7 C3 images (the left panel of Figure 1 shows one C2 image). We manually measured the location of the CME front along this line, and the velocity implied by each pair of consecutive height measurements is shown in the right panel of Figure 1.

The acceleration and match of the velocity and X-ray profiles are typical for a fast CME (e.g. the "intermediate acceleration" CME studied by Zhang et al., 2004). Although the exact dynamics are unclear (and not relevant here), it reaches a final speed of $1\,200$ km s^{-1} at 2016-05-15T17:06, at which point it has an elongation of $(2.56\pm0.03)°$. After this point it continues at near-constant speed, possibly slowly decelerating at a rate consistent with the 'Drag Based Model' of Vršnak et al. (2013).

4 Results

Once both standard and variability images had been produced for both observations, we are left with the common problem in astronomical imaging of identifying significant detections within our noisy images. For this, we used the widely used AEGEAN software package (Hancock et al., 2018) to identify sources in all 4 images. In all, 397 IPS sources were detected at 5σ in both variability and continuum in both observations. The g-level for each of these 397 sources was determined by computing the ratio of scintillation index between the target and reference observation. Figure 2 shows the g-levels obtained for our observation. The most obvious feature is a band of enhanced g-levels in the solar elongation range 32°–37°. These g-levels range from 1.3 to 1.9. In contrast, areas outside this area of enhancement have g-levels much closer to 1, except for occasional outliers.

We caution that at elongations $< 20°$ the IPS regime for the background solar wind is tending towards strong scintillation, which is associated with a saturation of the scintillation index at 1.0, thus the g-level metric is not sensitive to heliospheric structures closest to the Sun. However, for elongations beyond approximately 27°, sources can be expected to show a range of g levels from 0.5–2.0, so this should not affect our primary result.

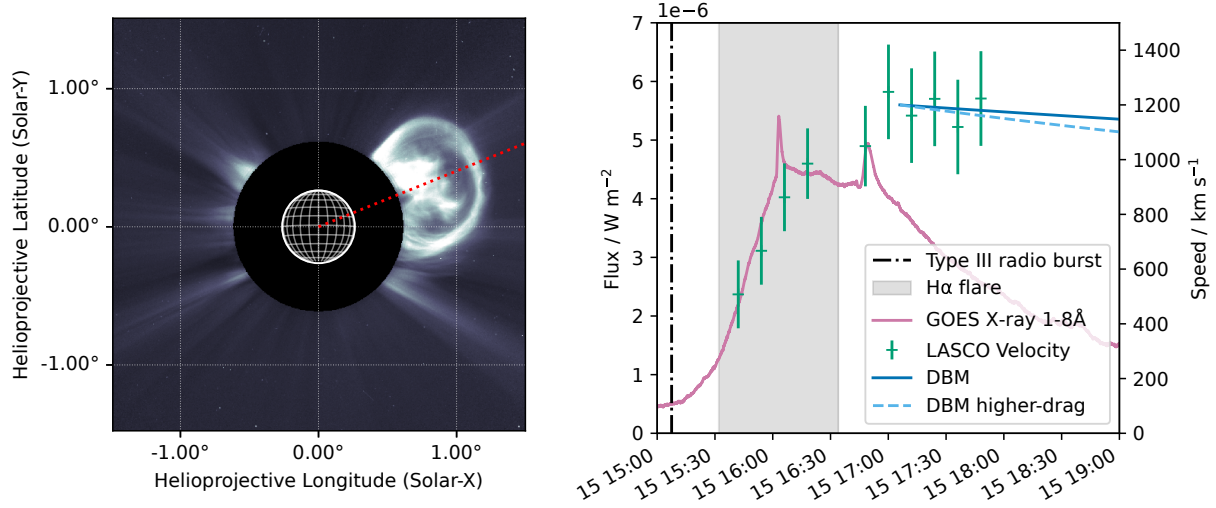As an alternative way to present these data, we also used these point measurements of the g-level to con-

Figure 1. Left panel: LASCO C2 image of the CME at 2016-05-15T16:12:06. Red dotted line indicates approximate axis of symmetry of CME, estimated from this figure. Right panel: CME velocity overlaid on X-ray flux. Dash-dot line indicates time of Type-III radio burst. Grey range indicates H-alpha flare. Each green velocity point is based on a pair of measurements of CME front location separated in time. Error bars are based on 20" error in C2 and 40" error in C3. Blue lines show velocity modelled using DBM (assuming plane of sky; see Sect. 5). Velocity and X-ray flux axes are scaled arbitrarily.

struct a 'g-map' using a Radial Basis Function (RBF), with the weight of each source being determined by the inverse square of distance (Epanechnikov, 1969)

$$w\left(r\right) = \begin{cases} 1 - \left(\frac{r}{5}\right)^2 & ; \ r < 5° \\ 0 & ; \ \text{otherwise} \end{cases} \quad (2)$$

where r is the distance of each source from the point of interest. Three contours of this g-map are shown in the top panel of Figure 2, to further illustrate the approximate extent of the area of enhanced scintillation.

The very high density of points (approximately 1 per square degree) in the MWA allow us to constrain the location and demarcate its extent. The region is extended tangentially to the Sun, with the bulk of the feature, and the highest g-values, lying below the centre line of the CME in the coronagraph images

4.1 Comparison with ISEE data

In the bottom panel of Figure 2 we compare our data with g-levels measured by the IPS facility operated by the Institute for Space-Earth Environmental Research in Japan (ISEE; Kojima & Kakinuma, 1990; Tokumaru, 2013). The ISEE array observes sources as they cross the local meridian, and we have marked the location of this meridian at the time of the MWA observation (thus sources close to the dotted line, including those in the region of enhanced g-levels, will have been observed near-contemporaneously with the MWA observation). One source inside the enhanced region (marked with a blue

square in the top panel of Figure 2) was observed by ISEE with the g-level of 2.17 providing an independent verification.

The ISEE array consists of 3 stations separated by ~ 100 km from which the velocity of the scintillation pattern (and hence the solar wind) can be derived. The source in our enhanced scintillation region has a velocity measurement of $453\,\text{km s}^{-1}$, compared to equatorial measurements off the Western limb of the Sun in days prior/post of around $300\,\text{km s}^{-1}$. Note, however, that no error is provided for these measurements, which means that only 2 stations were used. This means that errors (which are typically $\sim$10%) may be larger than usual, and therefore this measurement should not be given undue weight.

These ISEE data also drive the UCSD model (Jackson et al., 1998, 2020). The all-sky v-maps (velocity) and g-maps generated by this model show no sign of the CME. However, the velocity is consistently close to $300\,\text{km s}^{-1}$, at the times of both our reference and target observation and several days either side. We assume this velocity for the background solar wind throughout the rest of this paper.

4.2 MWA IPS Power Spectra

As well as the change in scintillation level, IPS time-series encode further information about the radio sources and scattering medium. Most notably, a higher trans-
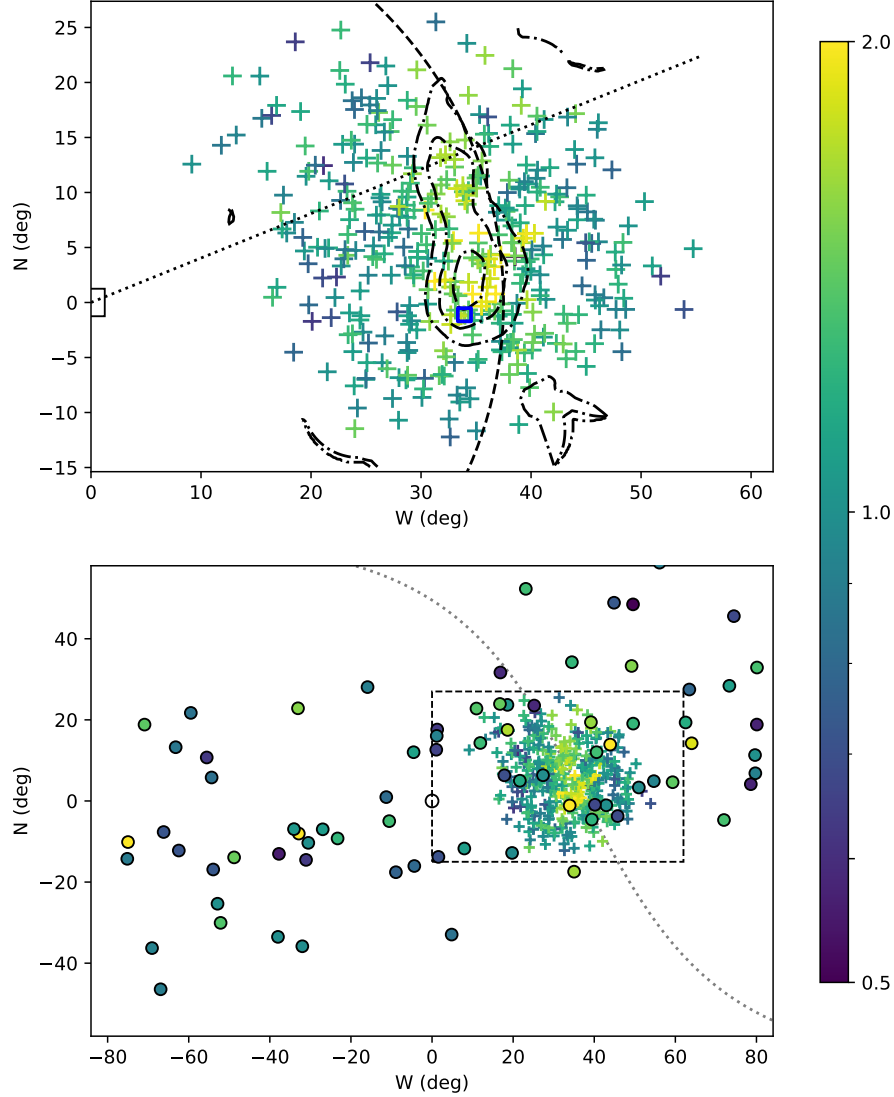
Figure 2. IPS observations in helioprojective coordinates. Top panel: sky map of g values derived from MWA data. Dotted line indicates direction of CME measured in LASCO images (i.e. red line in left panel of Figure 1). Dashed line indicates approximate location of the CME front (37.5°) estimated from this figure. Dash-dot lines are contours of smoothed g-value at 1.4, 1.5 and 1.6. Blue open square indicates location of ISEE source. Bottom panel: sky map with MWA g-levels (crosses) and ISEE g-levels (filled circles). Dotted line indicates location of ISEE meridian at the time of the MWA observation. Dashed rectangle indicates the boundary of the top panel, with the position of the Sun indicated by the open circle.
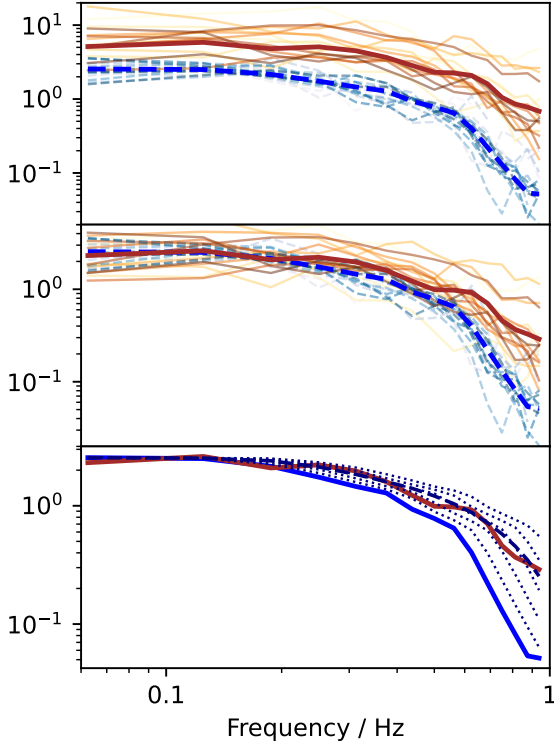
Figure 3. Top panel: power spectra for each source in the enhanced g region for the reference observation (in shades of blue), and target observation (in shades of brown). Darker shades are for sources with a higher S/N. Thick blue and brown lines are the average reference and target power spectrum respectively. Middle panel: same as top panel but target power spectra have been scaled by g^{-2}. Bottom panel: Average power spectra from 2nd panel. The Grey dotted lines are a set of reference power spectra scaled in frequency by factors of 1–1.6. Black dashed line is the average of the grey dotted lines.

verse velocity of the scattering screen will cause the scintillation signature to shift towards a higher frequency (Manoharan & Ananthakrishnan, 1990). Figure. 3 shows the power spectra corresponding to the 576 s timeseries, both in the target and reference observation, for those sources within the g=1.5 contour. Only 15 sources with S/N> 10 and scintillation index > 0.1 in the reference observation have been selected.

The power spectra were constructed as follows: for each source, for both target and reference observations, timeseries for the maximum-brightness pixel for each

source were extracted from each dataset, along with an off-source timeseries for a nearby pixel to provide a noise-level reference. Power spectra were then formed for each timeseries, and the off-source power spectra (all of which were checked to be consistent with white noise) were subtracted from the corresponding on-source power spectra. To permit comparison between different sources, all power spectra were normalised by the power spectrum from the reference observation in the range 0.25–0.5 Hz (thus, by construction, the reference power spectra all lie on top of each other). Note that variance due to ionospheric scintillation is typically two orders of magnitude weaker, and largely restricted to frequencies below 0.1 Hz (Waszewski et al., 2022), and so ionospheric effects are not expected to be visible.

The top panel shows both target and reference power spectra exactly as described above. All show the shape which is characteristic of weak scintillation (flat at low frequencies, followed by a power-law drop off above the "Fresnel Knee"). The variance has typically dropped by an order of magnitude by the Nyquist frequency of 1 Hz, but has not yet reached zero, so some high-frequency information has been lost. Nonetheless, there is sufficient information to make some simple observations.

It is clear that the target power spectra differ considerably from one to the next, however there is no obvious spatial trend to this variability. There also appears to be higher power at higher frequencies for the target power spectra. To demonstrate this more clearly, in the middle panel we have scaled the target power spectra by a factor of g^{-2}, so the remaining difference between the power spectra cannot be explained by the overall change in the scintillation amplitude.

As shown in the lower panel, if we take the average reference power spectrum, scale it in frequency by a range of factors between 1.1 and 1.6 (5 different scalings are plotted as dotted lines), and take the average (the bold dashed line) we end up with power spectrum resembling the target power spectrum. A physical interpretation for this is given in the following section.

5 Analysis

The estimation of 3D CME structure from 2D images requires care at longer solar elongations due to the complex geometry and underlying physics (e.g. Howard & Tappin, 2009). Changes in the CME morphology, or deviation from simple models, can easily lead to errors (e.g. Wood et al., 2010). Here, we restrict ourselves to simple geometrical arguments, and basic scintillation physics to provide some approximate constraints on the CME kinematics.
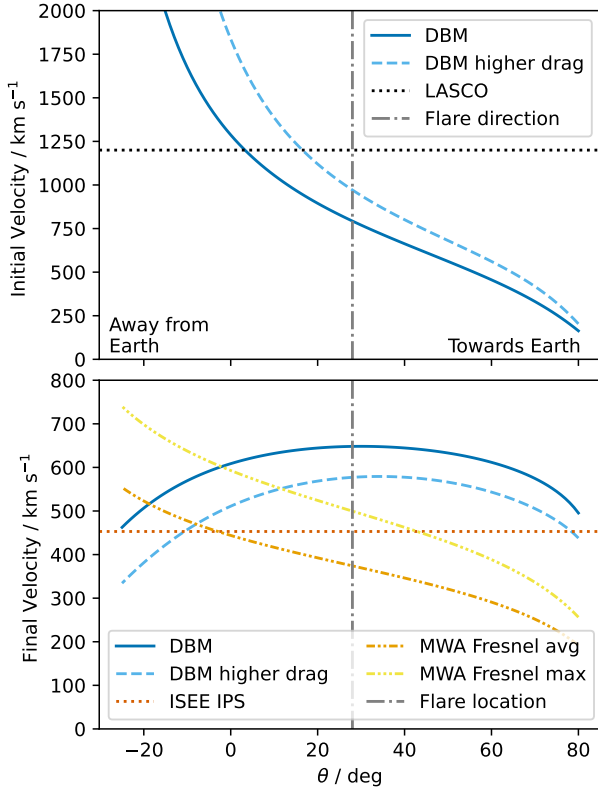
The location of the Hα solar flare gives a strong indication of the origin of the CME. Yashiro et al. (2008) found that although CMEs associated with flares launch on a radial trajectory on average, there is a distribution of position angle differences with a standard deviation of 18°. Thus, the discrepancy between a radial trajectory from the flare ($\phi \approx 10°$) and the LASCO-observed trajectory ($\phi = 22°$) is unremarkable, and there will be a similar uncertainty in the angle to the plane of sky, θ.

The main finding of our MWA observations is the location of the enhanced scattering, the leading edge of which lies at an elongation of approximately 37.5°. We now use the 'Drag-based Model' (DBM) of Vršnak et al. (2013) to confirm that this feature can be identified with CME detected previously in LASCO data. In the DBM, the kinematics of the CME are based purely on the background solar wind speed (w, which we assume to be 300 km s^{-1}, see Sect. 4.1) and a constant drag parameter, γ.

Under these assumptions, for a given, w, γ and θ, there is a unique initial velocity which will result in the CME traversing the direct path from an initial location close to the Sun (taken to be the point on the trajectory with $\epsilon = 2.56°$; see Sect. 3), to the final location on the MWA-observed line of sight. These implied initial velocities are plotted in the top panel of Figure 4, for a range of θ, for the prescribed value of γ for a strong, bright CME, and also for a slightly higher drag. The velocities have been projected into the plane of the sky to permit comparison with the coronagraph measurements. There is good agreement of these velocities with the LASCO launch velocity estimate of 1200 km s^{-1} (see Sect. 3) particularly for CME trajectories slightly closer to the plane of sky than suggested by the flare location.

A secondary finding is higher-than-ambient solar wind velocity in the heliosphere transient. This is suggested by the multi-station IPS measurement made by ISEE (see Sect. 4.1 and Figure 2); though as noted, this is rather weak evidence since only two stations were used and the errors may be large.

The excess higher-frequency power in the MWA scintillation is also suggestive of a higher screen velocity, since the scintillation timescale (τ_{scint}) is given by the Fresnel scale crossing time; i.e.

$$\tau_{\text{scint}} = r_F/v; \quad r_F = \sqrt{\frac{\lambda D}{2\pi}}, \tag{3}$$

where v is the velocity and r_F is the Fresnel scale, λ is the observing wavelength, and D is the distance from the observer (e.g. Narayan, 1993).

The single-station IPS velocity measurement technique of Manoharan and Ananthakrishnan (1990) introduced

Figure 4. Top panel: initial velocity, projected into the plane of the sky, required to carry a CME from the LASCO-observed location to the MWA-observed elongation under the assumptions of the drag-based model (c.f. Figure 1). Results are shown assuming the standard value of γ (=10^{-8} km^{-1}; solid line) and double that value (dashed line). Dotted line shows observed initial velocity. Lower panel: blue lines show the final velocity implied by the initial velocities, again projected into the plane of the sky (i.e. component normal to the line of sight at an elongation of 37.5°). Dotted red line shows velocity measured by multi-station IPS. Orange and yellow lines show the velocity implied by the mean (1.3) and max (1.6) frequency factors.

the method of measuring the shift in scintillation frequency and mapping this to a change in velocity. Below, we extend this idea slightly by noting that Equation 3 implies that a change in distance will also change the scintillation frequency. Thus, we aim to find which effective distance (and therefore which value of θ) gives the best consistency between our observed power spectra and other information on the likely velocity of the CME at the time of the IPS observation.

First we consider undisturbed solar wind which we presume is prevailing in the reference observation. In this case the scintillation signal will be dominated by the wind close to the point of closest approach, due to the steep drop in solar wind density as it expands away from the Sun (e.g. Coles & Rickett, 1976). Consequently, the reference power spectra are a weighted average of scintillation along the line of sight, but with the weighting function peaked at the piercepoint $D = \cos(\epsilon)$ AU (see, e.g. Rickett & Coles, 1991, Figure 1) and $v = 300$ km s^{-1} (see Sect. 3).

However, when a heliospheric transient such as a CME shock is traversing the line of sight, its density may exceed that at the piercepoint, thereby shifting the weighted average distance away from the piercepoint. Therefore, one interpretation of the bottom panel of Figure 3 is that v/r_F within the CME is between $1\times$ and $1.6\times$ higher than in the reference observation, averaged along and over different lines of sight. The detailed IPS study of a very energetic CME by Manoharan (2010) is instructive in interpreting this: when individual sources were observed over several hours as the full CME structure crosses the line of sight, power-spectrum velocity measurements ranged from CME speed to closer to ambient.

In the lower panel of Figure 4, we plot the final velocity implied by the initial velocities in the upper panel and the DBM model. As before, we project these velocities into the plane of the sky, this time for the line of sight of an observation offset by $37.5°$ from the Sun, to facilitate comparison with the IPS-derived velocities (This means that the velocities peak at $\theta = 37.5°$).

We also plot 'Fresnel velocities': velocities implied by the observed increase in the frequency of the scintillation between reference and target observations. Equation 1 gives a monotonic relationship between θ and D, and thereby r_F for our fixed value of ϵ, allowing us to solve for v in the target observation.

These IPS-derived velocities again favour a line of sight closer to the plane of sky ($\theta = 0$) than the solar flare location suggests. The average Fresnel velocity and multi-station velocity are in mild tension with the DBM according to this simple analysis. However, as noted by Tokumaru et al. (2021), this is to be expected since the

CME will only occupy part of the line of sight. These measurements are a weighted average over the entire line of sight and so will be regressed towards the ambient solar wind speed.

6 Discussion

As we have shown, the region of enhanced interplanetary scintillation can be identified with the LASCO-detected CME. The plane-of-sky velocity measured in the coronagraph images will carry the CME to the elongation observed with the MWA under reasonable assumptions. Trajectories slightly closer to the plane of sky and/or slightly lower drag are favoured compared to the radial trajectory implied by the solar flare location.

Our velocity estimates based on the average power spectrum are broadly consistent with the near-contemporaneous multi-station IPS measurement by ISEE, and can be made consistent with the kinematics implied by the location of the CME and the DBM propagation model. Likewise, the velocity analysis favours trajectories closer to the plane of sky and/or slightly lower drag.

However, this interpretation is not unique; for example, if the drag is higher closer to the Sun (and lower further away) then a more radial trajectory is consistent with our data. MWA IPS observations are ongoing, and in order to confirm the value of these observations, it will be necessary to assemble a larger sample of CME observations.

6.1 Future Work

In the current work we report on a case where the CME was detected only in a single observation, which leaves some ambiguity as to the northern extent of the CME. Since the MWA can be digitally steered to any point on the sky, in the future it will be possible to ascertain the extent of the CME more definitively, by extending our g-map using multiple pointings.

There are numerous possible approaches to determining CME speeds directly from our IPS data. The simple power spectrum approach demonstrated here is consistent with our other data; in particular the comparison with the multi-station IPS measurement (which is independent of the Fresnel scale) appears to rule out an Earth-bound trajectory. Secondly, once the individual MWA IPS sources are better understood, it will be possible to do more sophisticated power spectrum fitting to probe the turbulence properties, and the detailed morphology of a CME (e.g. Chang et al., 2021). Thirdly, Morgan et al. (2018) have shown that double radio sources (a common morphology) also allow the mea-

surement of the speed of the scintillation pattern, in an approach analogous to multi-station IPS. Finally, since the MWA is not limited to a daily observing cadence, it is also possible for us to measure the plane of sky motion of a CME over time. For example, had we observed our CME twice 2 hours apart, there would have been a shift in position of approximately $2°$, which would be easily measurable.

CME morphology in 3D has previously been modelled directly from IPS observations (Tokumaru et al., 2003; Tappin & Howard, 2010), and IPS data has also been used to select the best candidate from an ensemble of MHD models (Iwai et al., 2021). Such approaches should be directly applicable to our data.

Chhetri et al. (2022) have recently demonstrated that the ASKAP telescope, which is co-located with the MWA, and is similarly characterised by a wide field of view, is capable of making IPS observations. ASKAP's higher operating frequency ($700\,\mathrm{MHz}$–$1800\,\mathrm{MHz}$) makes it more suited to observing closer to the Sun, so that it should be possible to observe a CME at any distance from $\sim 5°$ outwards with the MWA and/or ASKAP. Utilising one or both these instruments, it will be possible to track a CME over a period of up to 12 hours, with thousands of sources all around the Sun being measured on an hourly cadence.

With a growing number of IPS-capable observatories world-wide, the heliosphere can be observed around the clock with a suite of instruments providing complementary information. Jackson et al. (2022) have recently shown that data from multiple IPS observatories can be synthesised together to reconstruct the inner heliosphere, using tomographic techniques; thus a priority will be to test how well MWA IPS data can drive such reconstructions (or MHD simulations; see e.g. Jackson et al., 2015).

Finally, this new capability has synergies with attempts to remotely sense the magnetic field orientation of a CME via Faraday rotation (see Kooi et al., 2022, for a recent review). Howard et al. (2016) stress the importance of tracers of CME density (for which IPS g-levels, like white-light coronagraph measurements, can act as a proxy). By providing detailed CME plane-of-sky morphology, at greater distance from the Sun, IPS increases the sky area over which Faraday rotation observations of a CME can be made. We note that our MWA IPS observations are also amenable to full polarimetric analysis (see e.g. Lenc et al., 2017, for a discussion of the polarimetric capabilities of the MWA), and that MWA observations can be used to generate an exquisite map of the ionospheric electron density (Loi et al., 2015; Jordan et al., 2017), a major contaminant of Faraday rotation observations (Oberoi & Lonsdale, 2012).

7 Open Research

The CACTus CME catalogue (Robbrecht et al., 2009) used for the initial cross-match described in Sect. 2.2 is available online (at `https://www.sidc.be/cactus/`)

Sunpy (SunPy Community et al., 2020) was used for coordinate conversions, as well as for downloading the GOES X-ray flux data as described in Sect. 3. We used Sunpy version 4.0.2 (Mumford et al., 2022). Sunpy was also used to retrieve Coronagraph images from `helioviewer.org`, including the one shown in the left panel of Figure 1. At the time, helioviewer was running release 3.4.0 (`https://github.com/Helioviewer-Project/api/releases/tag/3.4.0`).

Data from the ISEE IPS array is available in near-real time, with archival data going back many years. At the time of writing the ISEE data used in this paper can be found at the following URL: `https://stsw1.isee.nagoya-u.ac.jp/vlist/rt/nagoya.2016`. Reconstructions of velocity and g-level fields from the same data can be found at `ips.ucsd.edu` under the section "Archival 3D Imagery". The "fisheye" images use approximately the same coordinate system as used in this paper.

MWA data is available from the Australian Virtual Observatory `https://asvo.mwatelescope.org/`. At the time of writing the observations used in this paper are public, and can be identified by their GPS start times (1147479952 and 1147393800) which serve as unique identifiers of these observations within the MWA archive. All the IPS observations described in (Morgan et al., 2019) are also archived, under project code `D0011`.

Acknowledgments

References

Brueckner, G. E., Howard, R. A., Koomen, M. J., Korendyke, C. M., Michels, D. J., Moses, J. D., . . . Eyles, C. J. (1995, December). The Large Angle Spectroscopic Coronagraph (LASCO). Sol. Phys., *162*(1-2), 357-402. doi: 10.1007/BF00733434

Chang, O., González, R. F., Bisi, M. M., & Fallows, R. A. (2021, November). Observations of interplanetary scintillation of the 2005 May 13 coronal mass ejection: numerical models. MNRAS, *508*(1), 1314-1320. doi: 10.1093/mnras/stab2664

Chhetri, R., Morgan, J., Moss, V., Ekers, R., Scott, D., Bannister, K., . . . Shannon, R. M. (2022). First measurement of interplanetary scintillation with the askap radio telescope: implications for space weather. *Advances in Space Research*. doi: 10.1016/j.asr.2022.08.012

Clarke, M. (1964). *PhD Thesis* (Unpublished doctoral dissertation). Cambridge University. (ethos.bl.uk/OrderDetails.do?uin=uk.bl.ethos.597742)

Coles, W. A., & Rickett, B. J. (1976, September). IPS observations of the solar wind speed out of the ecliptic. J. Geophys. Res., *81*(25), 4797. doi: 10.1029/JA081i025p04797

Dennison, P. A., & Hewish, A. (1967, January). The Solar Wind outside the Plane of the Ecliptic. Nature, *213*(5074), 343-346. doi: 10.1038/213343a0

Dennison, P. A., & Wiseman, M. (1968, December). Preliminary Observations of the Effects of a Corotating Stream on Interplanetary Scintillation. PASA, *1*(4), 142-145. doi: 10.1017/S1323358000011103

Epanechnikov, V. A. (1969). Non-parametric estimation of a multivariate probability density. *Theory of Probability & Its Applications*, *14*(1), 153-158. doi: 10.1137/1114019

Gapper, G. R., Hewish, A., Purvis, A., & Duffett-Smith, P. J. (1982, April). Observing interplanetary disturbances from the ground. Nature, *296*(5858),

633-636. doi: 10.1038/296633a0

Gosling, J. T. (1993, November). The solar flare myth. J. Geophys. Res., *98*(A11), 18937-18950. doi: 10.1029/93JA01896

Hancock, P. J., Trott, C. M., & Hurley-Walker, N. (2018, March). Source Finding in the Era of the SKA (Precursors): Aegean 2.0. PASA, *35*, e011. doi: 10.1017/pasa.2018.3

Hewish, A., Scott, P. F., & Wills, D. (1964, September). Interplanetary Scintillation of Small Diameter Radio Sources. Nature, *203*(4951), 1214-1217. doi: 10.1038/2031214a0

Howard, T. A., Stovall, K., Dowell, J., Taylor, G. B., & White, S. M. (2016, November). Measuring the Magnetic Field of Coronal Mass Ejections Near the Sun Using Pulsars. ApJ, *831*(2), 208. doi: 10.3847/0004-637X/831/2/208

Howard, T. A., & Tappin, S. J. (2009, October). Interplanetary Coronal Mass Ejections Observed in the Heliosphere: 1. Review of Theory. Space Sci. Rev., *147*(1-2), 31-54. doi: 10.1007/s11214-009-9542-5

Iwai, K., Shiota, D., Tokumaru, M., Fujiki, K., Den, M., & Kubo, Y. (2021, December). Validation of coronal mass ejection arrival-time forecasts by magnetohydrodynamic simulations based on interplanetary scintillation observations. *Earth, Planets and Space*, *73*(1), 9. doi: 10.1186/s40623-020-01345-5

Jackson, B., Tokumaru, M., Fallows, R., Bisi, M., Fujiki, K., Chashei, I., . . . Bracamontes, M. (2022). Interplanetary scintillation (ips) analyses during lofar campaign mode periods that include the first three parker solar probe close passes of the sun. *Advances in Space Research*. Retrieved from https://www.sciencedirect.com/science/article/pii/S0273117722005002 doi: https://doi.org/10.1016/j.asr.2022.06.029

Jackson, B. V., Buffington, A., Cota, L., Odstrcil, D., Bisi, M. M., Fallows, R., & Tokumaru, M. (2020, November). Iterative Tomography: A Key to Providing Time- dependent 3-D Reconstructions of the Inner Heliosphere and the Unification of Space Weather Forecasting Techniques. *Frontiers in Astronomy and Space Sciences*, *7*, 76. doi: 10.3389/fspas.2020.568429

Jackson, B. V., Hick, P. L., Kojima, M., & Yokobe, A. (1998, June). Heliospheric tomography using interplanetary scintillation observations 1. Combined Nagoya and Cambridge data. J. Geophys. Res., *103*, 12049-12068. doi: 10.1029/97JA02528

Jackson, B. V., Odstrcil, D., Yu, H. S., Hick, P. P., Buffington, A., Mejia-Ambriz, J. C., . . . Tokumaru, M. (2015, February). The UCSD kinematic IPS solar wind boundary and its use in the ENLIL 3-D MHD prediction model. *Space Weather*, *13*(2), 104-115. doi: 10.1002/2014SW001130

Jordan, C. H., Murray, S., Trott, C. M., Wayth, R. B., Mitchell, D. A., Rahimi, M., . . . Morgan, J. (2017, November). Characterization of the ionosphere above the Murchison Radio Observatory using the Murchison Widefield Array. MNRAS, *471*(4), 3974-3987. doi: 10.1093/mnras/stx1797

Kaplan, D. L., Tingay, S. J., Manoharan, P. K., Macquart, J. P., Hancock, P., Morgan, J., . . . Williams, C. L. (2015, August). Murchison Widefield Array Observations of Anomalous Variability: A Serendipitous Night-time Detection of Interplanetary Scintillation. ApJ, *809*(1), L12. doi: 10.1088/2041-8205/809/1/L12

Kojima, M., & Kakinuma, T. (1990, August). Solar Cycle Dependence of Global Distribution of Solar Wind Speed. Space Sci. Rev., *53*(3-4), 173-222. doi: 10.1007/BF00212754

Kooi, J. E., Wexler, D. B., Jensen, E. A., Kenny, M. N., Nieves-Chinchilla, T., Wilson, I., Lynn B., . . . Manchester, W. B. (2022, April). Modern Faraday Rotation Studies to Probe the Solar Wind. *Frontiers in Astronomy and Space Sciences*, *9*, 841866. doi: 10.3389/fspas.2022.841866

Lenc, E., Anderson, C. S., Barry, N., Bowman, J. D., Cairns, I. H., Farnes, J. S., . . . Wayth, R. B. (2017, September). The Challenges of Low-Frequency Radio Polarimetry: Lessons from the Murchison Widefield Array. PASA, *34*, e040. doi: 10.1017/pasa.2017.36

Loi, S. T., Murphy, T., Cairns, I. H., Menk, F. W., Waters, C. L., Erickson, P. J., . . . Williams, C. L. (2015, May). Real-time imaging of density ducts between the plasmasphere and ionosphere. Geophys. Res. Lett., *42*(10), 3707-3714. doi: 10.1002/2015GL063699

Manoharan, P. K. (2010, August). Ooty Interplanetary Scintillation - Remote-Sensing Observations and Analysis of Coronal Mass Ejections in the Heliosphere. Sol. Phys., *265*(1-2), 137-157. doi: 10.1007/s11207-010-9593-5

Manoharan, P. K., & Ananthakrishnan, S. (1990, June). Determination of solar-wind velocities using single-station measurements of interplanetary scintillation. MNRAS, *244*, 691.

Morgan, J. S., Macquart, J. P., Chhetri, R., Ekers, R. D., Tingay, S. J., & Sadler, E. M. (2019, January). Interplanetary Scintillation with the Murchison Widefield Array V: An all-sky survey of compact sources using a modern low-frequency radio telescope. PASA, *36*, e002. doi: 10.1017/pasa.2018.40

Morgan, J. S., Macquart, J.-P., Ekers, R., Chhetri, R., Tokumaru, M., Manoharan, P. K., . . . Jackson, B. V. (2018, January). Interplanetary Scintillation with the Murchison Widefield Array I: a sub-

arcsecond survey over 900 deg^2 at 79 and 158 MHz. MNRAS, *473*, 2965-2983. doi: 10.1093/mnras/stx2284

Mumford, S. J., Freij, N., Stansby, D., Christe, S., Ireland, J., Mayer, F., . . . Murray, S. A. (2022, June). *Sunpy.* Zenodo. Retrieved from `https://doi.org/10.5281/zenodo.6727769` doi: 10.5281/zenodo.6727769

Narayan, R. (1993, January). The physics of pulsar scintillation. In J. M. Shull & H. A. Thronson (Eds.), *Pulsars as physics laboratories* (p. 151-165).

Oberoi, D., & Lonsdale, C. J. (2012, December). Media responsible for Faraday rotation: A review. *Radio Science*, *47*(6), RS0K08. doi: 10.1029/2012RS004992

Offringa, A. R., McKinley, B., Hurley-Walker, N., Briggs, F. H., Wayth, R. B., Kaplan, D. L., . . . Williams, C. L. (2014, October). WSCLEAN: an implementation of a fast, generic wide-field imager for radio astronomy. MNRAS, *444*(1), 606-619. doi: 10.1093/mnras/stu1368

Offringa, A. R., & Smirnov, O. (2017, October). An optimized algorithm for multiscale wideband deconvolution of radio astronomical images. MNRAS, *471*(1), 301-316. doi: 10.1093/mnras/stx1547

Rickett, B. J., & Coles, W. A. (1991, February). Evolution of the solar wind structure over a solar cycle: Interplanetary scintillation velocity measurement compared with coronal observations. J. Geophys. Res., *96*(A2), 1717-1736. doi: 10.1029/90JA01528

Robbrecht, E., & Berghmans, D. (2004, October). Automated recognition of coronal mass ejections (CMEs) in near-real-time data. A&A, *425*, 1097-1106. doi: 10.1051/0004-6361:20041302

Robbrecht, E., Berghmans, D., & Van der Linden, R. A. M. (2009, February). Automated LASCO CME Catalog for Solar Cycle 23: Are CMEs Scale Invariant? ApJ, *691*(2), 1222-1234. doi: 10.1088/0004-637X/691/2/1222

Shaifullah, G., Tiburzi, C., & Zucca, P. (2020, October). CMEchaser, Detecting Line-of-Sight Occultations Due to Coronal Mass Ejections. Sol. Phys., *295*(10), 136. doi: 10.1007/s11207-020-01705-0

SunPy Community, Barnes, W. T., Bobra, M. G., Christe, S. D., Freij, N., Hayes, L. A., . . . Dang, T. K. (2020, February). The SunPy Project: Open Source Development and Status of the Version 1.0 Core Package. ApJ, *890*(1), 68. doi: 10.3847/1538-4357/ab4f7a

Tappin, S. J. (1986, January). Interplanetary scintillation and plasma density. Planet. Space Sci., *34*, 93-97. doi: 10.1016/0032-0633(86)90106-6

Tappin, S. J., & Howard, T. A. (2010, August). Reconstructing CME Structures from IPS Observa-

tions Using a Phenomenological Model. Sol. Phys., *265*(1-2), 159-186. doi: 10.1007/s11207-010-9588-2

Tingay, S. J., Goeke, R., Bowman, J. D., Emrich, D., Ord, S. M., Mitchell, D. A., . . . Wyithe, J. S. B. (2013, January). The Murchison Widefield Array: The Square Kilometre Array Precursor at Low Radio Frequencies. PASA, *30*, e007. doi: 10.1017/pasa.2012.007

Tokumaru, M. (2013, January). Three-dimensional exploration of the solar wind using observations of interplanetary scintillation. *Proceedings of the Japan Academy, Series B*, *89*(2), 67-79. doi: 10.2183/pjab.89.67

Tokumaru, M., Fujiki, K., Kojima, M., & Iwai, K. (2021, November). Global Distribution of the Solar Wind Speed Reconstructed from Improved Tomographic Analysis of Interplanetary Scintillation Observations between 1985 and 2019. ApJ, *922*(1), 73. doi: 10.3847/1538-4357/ac1862

Tokumaru, M., Kojima, M., Fujiki, K., Yamashita, M., & Yokobe, A. (2003, May). Toroidal-shaped interplanetary disturbance associated with the halo coronal mass ejection event on 14 July 2000. *Journal of Geophysical Research (Space Physics)*, *108*(A5), 1220. doi: 10.1029/2002JA009574

Vršnak, B., Žic, T., Vrbanec, D., Temmer, M., Rollett, T., Möstl, C., . . . Shanmugaraju, A. (2013, July). Propagation of Interplanetary Coronal Mass Ejections: The Drag-Based Model. Sol. Phys., *285*(1-2), 295-315. doi: 10.1007/s11207-012-0035-4

Waszewski, A., Morgan, J., & Jordan, C. H. (2022, September). A measurement of small-scale features using ionospheric scintillation. Comparison with refractive shift measurements. PASA, *39*, e036. doi: 10.1017/pasa.2022.33

Wood, B. E., Howard, R. A., & Socker, D. G. (2010, June). Reconstructing the Morphology of an Evolving Coronal Mass Ejection. ApJ, *715*(2), 1524-1532. doi: 10.1088/0004-637X/715/2/1524

Xie, H., Ofman, L., & Lawrence, G. (2004, March). Cone model for halo CMEs: Application to space weather forecasting. *Journal of Geophysical Research (Space Physics)*, *109*(A3), A03109. doi: 10.1029/2003JA010226

Yashiro, S., Michalek, G., Akiyama, S., Gopalswamy, N., & Howard, R. A. (2008, February). Spatial Relationship between Solar Flares and Coronal Mass Ejections. ApJ, *673*(2), 1174-1180. doi: 10.1086/524927

Young, A. T. (1971, September). Interpretation of Interplanetary Scintillations. ApJ, *168*, 543. doi: 10.1086/151108

Zhang, J., Dere, K. P., Howard, R. A., & Vourlidas, A. (2004, March). A Study of the Kinematic Evolution of Coronal Mass Ejections. ApJ, *604*(1), 420-432. doi: 10.1086/381725